Fluorescence-based mapping of dielectric permittivity of condensates and their environment

E. Sabri, A. Mangiarotti and R. Dimova

Max Planck Institute of Colloids and Interfaces, Science Park Golm, 14476 Potsdam, Germany

ABSTRACT

Membraneless organelles, formed through liquid-liquid phase separation, are essential for cellular organization and function. Their dielectric permittivity (or micropolarity) influences viscosity, structural integrity, protein conformations, and hydration. Large permittivity contrasts between condensates and their surrounding medium lead to high interfacial tension, affecting their stability and interactions with membranes and other cellular structures. While environment-sensitive fluorophores are commonly used to probe condensate micropolarity, precise permittivity measurements remain challenging, as existing approaches have limited dynamic ranges and fail to resolve both dense and dilute phases, especially in systems with high permittivity differences. Additionally, calibration curves are solvent-dependent, complicating reproducibility. Here, we introduce a broadband fluorescence-based method using ACDAN, a water-soluble dye that shifts fluorescence based on local polarity, allowing direct permittivity measurements. Using this approach, we reveal an unexpectedly wide permittivity range ($5\varepsilon_0$ to $70\varepsilon_0$) within condensates, suggesting substantial polarity differences that influence molecular partitioning and condensate-membrane interactions. Importantly, this method enables simultaneous measurement of protein-rich and protein-depleted phases, providing a direct readout of a mixture's position on its phase diagram. Because it relies on fluorescence imaging, this technique is highly versatile for studying condensates in both live-cell and in vitro systems demonstrating robustness across microscopy and spectroscopy platforms. Our technique offers a powerful tool for probing dielectric properties in biomolecular condensates and other microheterogeneous systems, revealing new insights into their biophysical regulation and function.

INTRODUCTION

Biomolecular condensates form as a result of liquid-liquid phase separation (LLPS) and are key to intracellular organization. Examples of these phase-separated compartments include membraneless organelles such as stress granules [1], nucleoli [2], mitochondrial nucleoids [3] and nuclear speckles [4], which provide a dynamic and reversible means for cells to maintain homeostasis [1, 3, 4], adapt to stress [5-7] and regulate biochemical processes spatially and temporally [4, 8, 9]. The unique biophysical properties of condensates, such as viscosity [10, 11], protein packing [12, 13], hydration [7, 14, 15], pH [16] and interfacial properties [17], set them apart from their surrounding environment.

Among the various techniques used to study these properties, fluorescence-based imaging has emerged as a powerful tool due its sensitivity, non-invasiveness and high spatial and temporal resolution [11, 18-21]. Notably, polarity-sensitive dyes have proven efficient for probing how changes in protein sequence and interactions influence condensate properties *in vitro* and *in vivo* [11]. Importantly, polarity itself has been recognized as a general metric for condensate material properties correlating strongly with viscosity [11, 21] and surface tension [2, 11, 21].

Despite their advantages, existing techniques come with limitations. Fluorescent lifetime imaging (FLIM), for instance, requires long acquisition durations to map the polarity of the dilute phase of condensate systems and important data-storage capacity [11, 18-21]. Additionally, polarity measurements are often quantified in terms of dielectric permittivity (ε), which spans a broad range (from ~$2\varepsilon_0$ for oils and membrane core to ~$80\varepsilon_0$ for water), yet most fluorescence techniques operate on a truncated scale typically covering up to $55\varepsilon_0$ [11, 21-26]. Further challenges arise from relying on empirical calibration curves derived from a single type of binary mixtures [11, 21], which can lead to inconsistencies across different systems and experimental setups. These limitations hinder the accuracy and reproducibility of condensate polarity measurements.

In this study, we introduce a robust fluorescence-based method for quantifying the dielectric permittivity of biomolecular condensates and their environment using 2-acetyl-6-(dimethylamino)naphthalene (ACDAN), a dipolar relaxation-sensitive dye from the di-methylaminonaphthalene (DAN) family [27, 28]. ACDAN has been extensively used to characterize intracellular water activity [29-31], macromolecular crowding [32] and membranous compartments [28, 33]. Here, we extend its application demonstrating that ACDAN's spectral response can be systematically and consistently calibrated across a wide range of solvents, experimental conditions and equipment.

By combining spectrofluorimetry (cuvette-based measurements) with confocal hyperspectral imaging (microscopy), and employing analytical approaches such as phasor analysis and Gaussian interpolation, we demonstrate that ACDAN emission redshift provides a robust and quantitative permittivity readout for a broad panel of solvents. Our method enables the permittivity measurement of both the condensates and their surrounding solution simultaneously, offering a general tool for assessing the degree of phase separation in condensates systems. Lastly, we illustrate how our approach can be applied to quantify changes in condensate properties in response to the addition of ATP, a well-known hydrotrope [34], elucidating the role of water versus protein in determining the dielectric environment within condensates. Because our method is fluorescence-based, it can be readily implemented in any laboratory equipped with moderate microscopy instrumentation, making it widely accessible for studying biomolecular condensates and other microheterogeneous systems.

RESULTS

Spectrofluorimetry of ACDAN provides a sensitive readout of solvent permittivity

ACDAN has been reported to have a strong sensitivity to the polarity of the solvent (citations). The mechanism that explains such sensitivity is called solvent relaxation, also known as dipolar relaxation, as illustrated by the Perrin-Jablonsky diagram presented in Fig. 1a. Upon UV absorption, the dipole moment of ACDAN increases. In response, surrounding solvent molecules reorient in order to screen the excess charge induced by the excited-state dipole, thus minimizing the overall energy of the dye-solvent system. This energy minimization results in a red-shift of the dye fluorescence emission that scales with the solvent permittivity (polarity). These spectral shifts can be measured via spectrofluorimetry or hyperspectral imaging (see Fig. S1 in the supplementary information, SI). However, while spectrofluorimetry offers high spectral resolution, it captures the bulk fluorescence response of a solution without spatial differentiation. In contrast, hyperspectral imaging provides spatially resolved spectral information, enabling the mapping of permittivity variations within heterogeneous samples, as demonstrated further below.

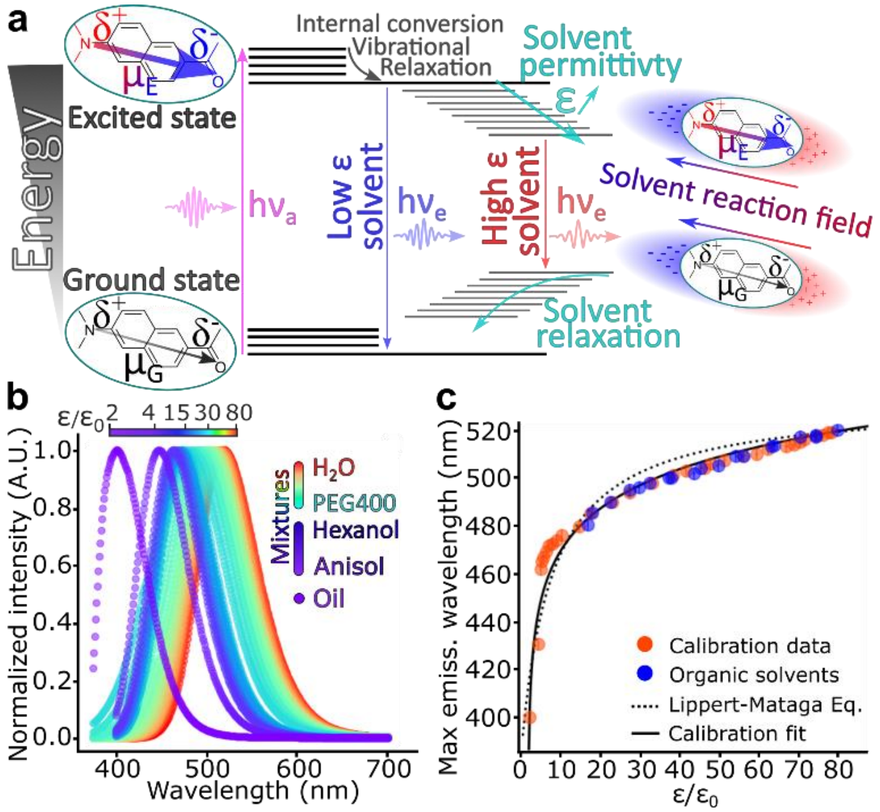

Figure 1: Calibration of ACDAN spectroscopy for solvent permittivity measurements. (a) Perrin-Jablonsky diagram illustrating the dependence of ACDAN fluorescence on solvent permittivity. The molecular structure of ACDAN and schematic illustration of its dipole moment change are depicted in the sketches. Highly polar solvents lead to red shift in the dye fluorescence, while low-polarity solvents cause a blue shift. **(b)** Spectrofluorimetry measurement of ACDAN fluorescence in various homogeneous solvents including mineral oil, mixtures of anisol and 1-hexanol (0%, 12%, 23%, 34%, 45%, 55%, 64%, 74% and 100% anisol content) and PEG-400 solutions in water (0%, 0.5%, 1%, 2%, 4%, 6%, 8%, 10%, 15%, 20%, 25%, 30%, 35%, 40%, 45%, 50%, 60%, 70%, 80%, 90% and 100% PEG content). The color bar represents the dielectric constants of these mixtures taken from the literature [35-37] and summarized in Table S1 of the supplementary information. **(c)** Calibration curve (solid circles) showing the maximum emission wavelength of ACDAN as a function of the dielectric constant of calibration solutions (orange) introduced in panel (b). The data points represent individual measurements; each point is mean±SD (n=3). Additional data (blue) include dioxane-water mixtures (5%, 15%, 25%, 35%, 45% and 55% dioxane content), ethanol-water mixtures (5%, 15%, 20%, 30%, 40%, 50%, 60%, 70%, 80%, 90% and 100% ethanol content), and butanol for which the emission spectra are given in Fig. S2 in the SI. The permittivities of all mixtures are literature values [36, 38], except for the ethanol-water mixtures, which were computed using the Maxwell-Garnett law of mixtures (see Table S4 in the SI for details). The dotted and solid lines respectively represent the Lippert-Mataga equation (Eq. 1) and a logarithmic fit function (Eq. 2).

Figure 1b shows the fluorescence emission of ACDAN in different solvents and homogeneous mixtures with permitivities ranging from 2 to 80. To quantify the relationship between spectral shifts and solvent permitivitty, we use a modified version the well-established Lippert-Mataga equation that correlates solvent general polarizability with the Stokes shift of a solvated dye [39]. The model assumes a spheroidal geometry for the dye molecule [40], allowing the maximum emission wavenumber ν to be approximated as:

$$\nu \sim \mu_E \frac{(\mu_G - \mu_E)}{V_{dye} hc} f(\epsilon) + \text{const}, \tag{1}$$

where ϵ is the solvent permittivity, μ_E and μ_G are excited state and ground state dipole moments of the fluorophore, V_{dye} is the effective molecular volume of ACDAN, h is the Planck constant, c is the speed of light in vacuum, and $f(\epsilon)$ is the generalized Debye function (full derivation is given in the SI). Given the relation $\nu = \frac{1}{\lambda_{max}}$, with λ_{max} being the wavelength of peak emission, Fig. 1c shows the qualitative agreement between Eq. 1 (used as a fit function) and our experimental data. The origin of the partial offset between the theoretical predictions and experimental results is discussed in the SI.

To further refine our calibration, we found that a logarithmic fit function provided the best empirical agreement with our data:

$$y = C_1 \ln(x + C_2) + C_3, \tag{2}$$

where C_i are fitting constants. Table S2 lists all fitting parameters used across different datasets in this study. To validate our calibration curve (Fig. 1c), we used dioxane-water and ethanol-water mixtures in various ratios with well-documented permittivities. The emission spectra of these solutions are presented in Fig. S2a-b. Table S3 compares the permittivities of benchmark organic solvent mixtures reported in the literature with those derived from the calibration curve in Fig. 1c.

Hyperspectral imaging and spectrofluorimetry of ACDAN yield comparable sensitivity to solvent permittivity

While spectrofluorimetry allows an accurate determination of solvent permittivity using ACDAN, it is limited to bulk (cuvette) measurements, without spatial resolution. Hyperspectral imaging overcomes this limitation by combining fluorescence microscopy with spectral analysis, capturing the emission spectra at each pixel to map local permittivity variations. To analyze the spectral data from the pixels in the image stacks, we used two approaches: Gaussian fitting and phasor plot analysis via the discrete Fourier transform (DFT) [32]. Figure 2 illustrates how emission spectra can be translated into a spatially resolved measure of the permittivity of the dye microenvironment.

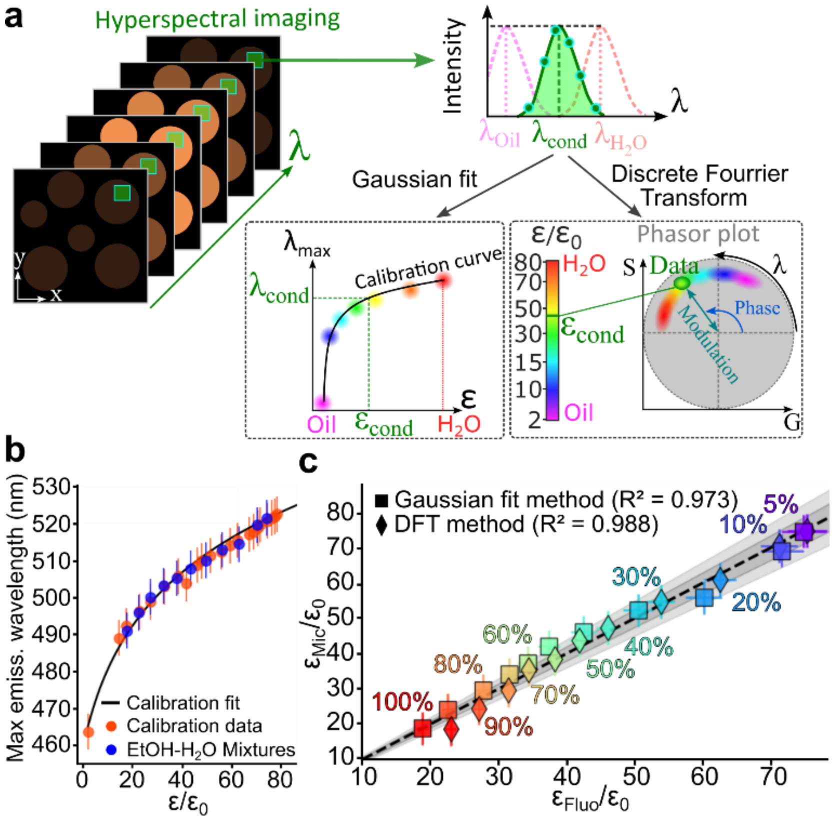

Figure 2: Hyperspectral imaging allows the spatial mapping of solvent permittivity with pixel resolution. (a) Schematic representation of 2D confocal microscopy hyperspectral stack analysis performed on a sample with biomolecular condensates. The local permittivity in a pixel of the image is determined based on prior calibration, using two different approaches (illustrated by different colors in the left inset and by the color bar and data clouds in the right inset), see text for details. **(b)** Calibration curve of the maximum emission wavelength as a function of solvent dielectric constant obtained using the Gaussian fit method. The H_2O-EtOH mixtures contain ethanol at 5%, 10%, 20%, 30%, 40%, 50%, 60%, 70%, 80%, 90% and 100%. **(c)** Cross-comparison of permittivity measurements for the H_2O-EtOH mixtures introduced in (b) comparing values obtained using the DFT (diamonds) and Gaussian fit (squares) approaches show strong agreement ($R^2 > 0.97$ for a linear correlation). Data acquired using a fluorimeter (horizontal axis) and microscopy (vertical axis). The color of the symbols represents ethanol concentration corresponding to the respective volume percentages indicated. The light grey and dark grey regions are guides to the eye that respectively represent 10% and 5% error intervals from the reported values.

The Gaussian fit approach consists in fitting the spectral data in each pixel with a skewed Gaussian function (Figs. 2a and S1). The peak position of this function is then mapped to a local permittivity value using Eq. 2-type calibration curve as presented in Fig. 2b. The DFT method on the other hand applies a discretized Fourier transform to the dye emission spectrum, representing it as a point in a two-dimensional "phasor plot" (Fig. 2a, left graph). The coordinates correspond to the real (G) and imaginary (S) components of the DFT. While the modulation provides information on the broadness of the spectrum, which can be affected by, e.g., fluorescence quenching [39], the phase reflects the emission spectrum center of mass, which depends on the permittivity of fluorophore microenvironment [32].

Consequently, the spectral data from an image yields a scatter plot in the phasor space (as sketched in Fig. 2a). To establish a calibration, we analyzed images of homogeneous solutions of known permittivity, generating a reference phasor plot (see Fig. S3a,c). The relation between the average phase of each solution and its permittivity was then fitted with an Eq. 2-type function yielding a DFT-based calibration curve (see Fig. S3d). Similarly, applying the DFT approach to spectrofluorimeter-acquired emission spectra of ACDAN in solutions of known permittivity allowed us to construct an independent permittivity calibration curve (see Fig. S2c,d).

To validate the equivalence of these approaches, Fig. 2c shows a comparison of the permittivity measurements for water-ethanol mixtures obtained using the DFT and Gaussian fit approaches across different instruments (microscope versus spectrofluorimeter). Despite the different calibration curve profiles that can be expected between instruments [41] (compare Figs. 1c and 2b), the results from methods aligns very well, presenting high coefficients of determination ($R^2 > 0.97$). This confirms the equivalence of the Gaussian fit and phasor-based approaches.

Additionally, the consistency presented in Fig. 2c also underscores the instrumental versatility of the calibration methods proposed. Notably, ACDAN emission provides a broadband readout of solvent permittivity $(2-80\varepsilon_0)$ with consistent accuracy across diverse solvents underscoring the approach robustness.

In the following, we employ the microscopy-based DFT approach (calibration detailed in Fig. S3) to resolve the permittivity of biomolecular condensates. This method was chosen for its superior accuracy among all approaches, with maximum error of 8% (see Table S4).

Hyperspectral imaging allows determination of biomolecular condensates permittivity

We focused on six different systems undergoing distinct type of LLPS: (i) segregative LLPS in polyethylene-glycol (PEG)–bovine serum albumin (BSA), and PEG–dextran solutions, (ii) self-coacervation in myelin basic protein (MBP) and soy-plant based glycinin condensates, and (iii) complex coacervation in adenosine triphosphate (ATP)–polydiallyldimethylammonium chloride (PDDA), and oligopeptides-based condensates made of poly-lysine (K)–poly-aspartic acid (D) (K_{10}-D_{10}) and poly-arginine (K)–poly-aspartic acid (D) (R_{10}-D_{10}). The results of the DFT-based analysis of hyperspectral stacks for these systems are presented in Fig. 3.

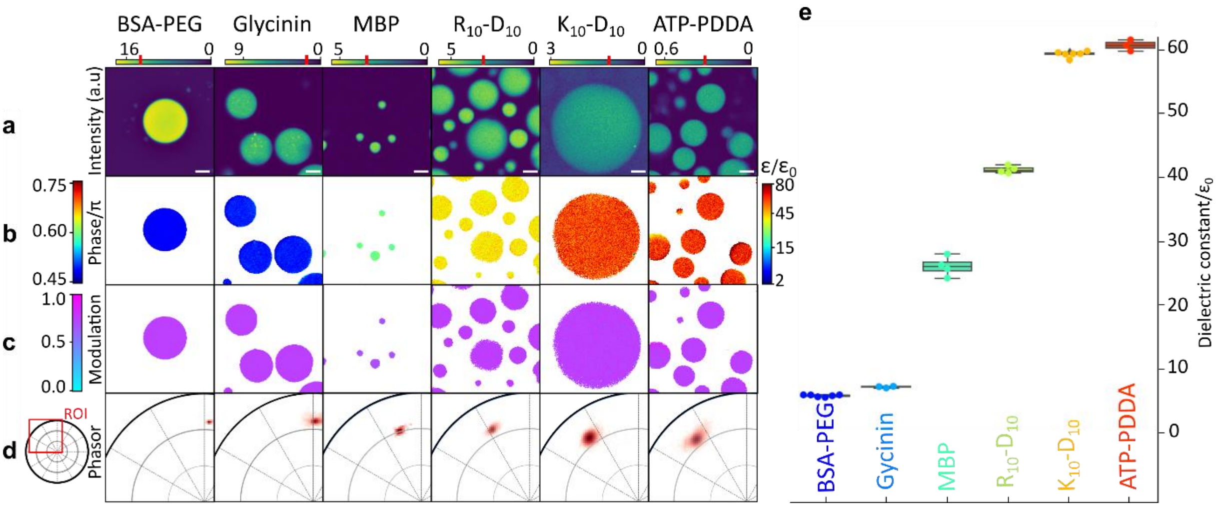

Figure 3: ACDAN hyperspectral imaging enables the determination of biomolecular condensate permittivity. **(a)** Mean intensity of a stack of hyperspectral images of different condensate systems, labeled at the bottom of the figure. The color bars (arbitrary units) represent fluorescence intensity, with the red marks indicating the threshold below which pixels were excluded from the analysis. The scale bars represent 5µm. **(b)** Phase of the spectral signal (see Fig. 2a and Methods section) with values presented on the left color bar. Using the microscopy-based DFT calibration curve (Fig. S3), these values are translated into permittivity values shown on the color bar on the right. **(c)** Modulation of the spectral signal (see Fig. 2a and Methods section) with values displayed on the left color bar. **(d)** Phasor plot representation of the spectral information from each image stack shown as a 2D scatter plot where each dot on the phasor plot shows the phase and modulation of each individual pixel. The inset on the left highlights the region of interest (ROI) covering the experimental permittivity range of the data (from $2\epsilon_0$ to $80\epsilon_0$). **(e)** Rescaled permittivity values for all condensate systems imaged in (a) where each dot

represents a stack of images. Box plots indicate mean±SD (BSA-PEG and K_{10}-D_{10}: n=6, glycinin, ATP-PDDA: n=3, R_{10}-D_{10} and MBP: n=4), additional statistical details are provided in Fig. S4.

Note that panels (b-d) of Fig. 3 were produced applying a minimal intensity threshold to filter the highest intensity portion of the data in panel A. This procedure distinguishes condensates that were already at the bottom of the experimental chamber from the onset of image acquisition (highest mean signal) from those that sedimented in the observation zone during acquisition (moderate to low mean signal). The latter exhibited artificially high permittivity due to absence of shorter wavelength components of their spectra and were therefore excluded from the analysis.

Figure 3b-c shows that while phase values (related to the emission maximum) and thus permittivity (inset b) vary among condensates systems, the modulation (related to the spectra broadness) only slightly decreases with increasing permittivity (Fig. 3c). This is further evident in Fig. 3d and is consistent with expected fluorescence quenching effect associated with dipolar relaxation [39]. The spread of the pixel cloud in Fig. 3d provides a visual estimate of the measurements error, which is proportional to the photon signal-to-noise ratio.

Averaging the phase values and converting them to permittivity for different trials yields Fig. 3e (additional statistical details are provided in Fig. S4). Importantly, the weak correlation between the type of interaction driving LLPS and condensate permittivity (Fig. 3e), suggest that condensate dielectric properties cannot be predicted solely based on the chemical nature of the components and the type of LLPS. A striking example is the comparison between K_{10}-D_{10} and R_{10}-D_{10} condensates: despite differing only by four atoms in a single amino acid, their permittivities differ drastically, i.e. by $20\epsilon_0$ (see Fig. 3e).

Hyperspectral imaging of condensate permittivity provides a fingerprint for the condensate phase state

Upon changes in polymer concentration within either region of a phase separated system, variation in protein hydration and water activity alter the permittivity contrast between the two phases [2, 11, 42]. These changes are best understood thermodynamically as a concentration-dependent shift in the system position on its phase diagram [43]. From this perspective, measuring the permittivity contrast between two aqueous phases provides a direct readout of the phase state of a mixture, enabling the extraction of key parameters such as interfacial tension [44]. This becomes particularly important when investigating the fundamental origin of interfacial tension mediated biologically relevant phenomena, such as the wetting of membranes by biomolecular condensates [45, 46].

Figure 4 presents how the sensitivity of this approach can be used to further distinguish different points on the phase diagram of a given mixture.

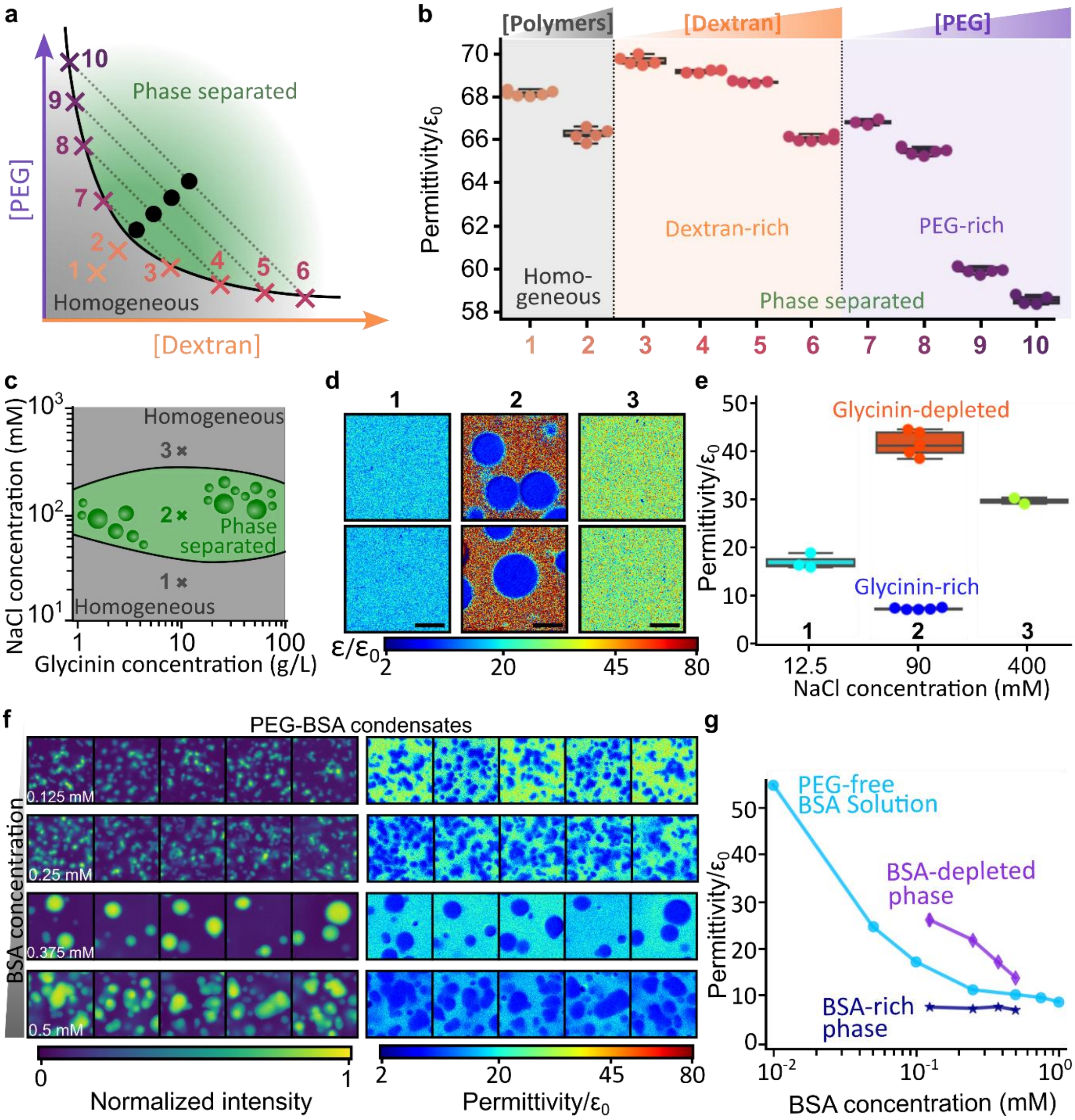

Figure 4: Hyperspectral imaging of condensate permittivity enables mapping of phase diagram positions. (a) Sketch of the PEG-Dextran phase diagram, see [43] for experimental values. Points (1-2) correspond to homogeneous PEG-Dextran mixtures. The black dots exemplify phase separated mixtures with points (3-10) positioned along the binodal (black curve). The tie lines (dotted lines) connect the coexisting phases where points (3-6) represent the compositions of the dextran-rich phases and points (7-10) represent the compositions of the PEG-rich phases. The total weight fractions of PEG and dextran used to prepare the solutions in this work are given in Fig. S5. **(b)** Hyperspectral imaging measurement of the permittivity of the PEG-dextran mixtures presented in (a), see Fig. S5 for exact compositions. **(c)** Phase diagram of glycinin condensation as a function of protein and NaCl concentrations [47]. The grey regions represent homogeneous mixtures and the green region denotes conditions of phase separation, i.e. condensate formation. Points 1, 2 and 3 correspond to NaCl concentrations of 12.5, 90, and 400 mM, respectively, with a constant protein concentration of 10 g/L. **(d)** Permittivity maps corresponding to the three different salt concentrations marked by points 1, 2 and 3 in (c); examples from two different regions of the same sample. The color bar represents the rescaled permittivity. **(e)** Quantified permittivity of all different phases at points 1, 2 and 3 in (c,d). **(f)** Imaging the impact of BSA concentration on the permittivity of PEG-BSA condensate systems (examples from five different regions of the sample are given). The left panel shows average intensity maps of hyperspectral stacks for different initial BSA concentrations (indicated in white), and the right panel displays the

corresponding permittivity maps of the samples presented on the left. **(g)** Influence of increasing the total BSA concentration on the permittivity of homogeneous protein solutions in water (blue points), and BSA-rich phase (stars) and BSA-depleted phase (diamonds) of PEG-BSA condensate systems.

Figure 4a,b shows how variations in the initial concentrations of PEG and dextran, as schematically defined by the points in the phase diagram of panel a, translate into different permittivity values of the solutions in each condition. Even small increase in polymer concentrations (a few tens of percent), consistently results in lower permittivity, consistent with previous reports [35]. Measurements of points (3-10) in Figs. 4a,b were performed by isolating each phase of the PEG-dextran mixtures, with permittivity maps and initial concentrations given in Fig. S5.

Figures 4c-e,f,g further emphasize the generality of these trends for glycinin at varying NaCl concentrations and PEG-BSA condensates, respectively. Figure 4c-e shows that different points in the glycinin phase diagram correspond to markedly different permittivity values between the homogeneous and the phase separated states. Similarly, Fig. 4f shows that increasing the overall BSA concentration decreases the permittivity of the BSA-depleted phase, a trend quantified in Fig. 4g and compared to PEG-free BSA aqueous solutions. Given that BSA is the main hydrophobic component of the mixture, this representation allows a qualitative estimate of BSA concentration in different regions of the phase-separated system (the permittivity map of the BSA solutions used in Fig. 4g is provided in Fig. S6). Since enzymatic activity requires a high-permittivity hydrogen-bonded water network at the enzyme surface to remain biologically active [48, 49], the results of Fig. 4 align with reports of decreased enzymatic activity in the condensed phase of PEG-BSA mixtures compared to homogeneous BSA solutions of similar overall concentrations [50]. Figure S7 presents a similar comparison for glycinin, contrasting salt-free glycinin solutions with the two phases of its phase-separated counterpart (i.e., point 2 in Fig. 4c-e). Overall, these findings emphasize that the presented method enables systematic, single-measurement quantification of permittivity of both the protein-rich and protein-depleted phases, representing a strong novel advancement of this work.

Hyperspectral mapping shows how ATP modulates condensate permittivity through hydrotropic effects

Above, we demonstrated that permittivity provides a distinct fingerprint for the phase state of a given condensate system. To assess the sensitivity of out method to chemically induced changes, we investigated the effects of hydrotropes – molecules known to enhance protein hydration [34, 51, 52]. Specifically, we examined the impact of ATP, a well-established hydrotrope, on condensate permittivity. Figure 5 shows that the presence of these molecules significantly alters the permittivity of different condensate systems, highlighting the method capability to detect subtle physicochemical changes in the microenvironment.

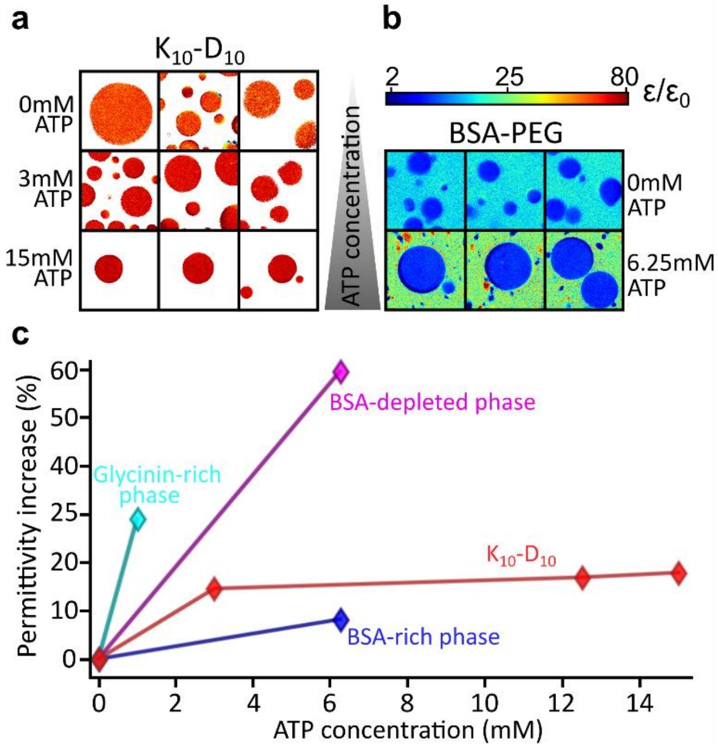

Figure 5: Hyperspectral mapping of condensate permittivity reveals the hydrotropic effect of ATP. **(a-b)** Permittivity maps illustrating the effect of increasing ATP concentration on K_{10}-D_{10} and BSA-PEG condensates, respectively. Each frame represents a 36.9x36.9µm^2 sample area with the color bar in (shown in b) indicating permittivity on a logarithmic scale. In (a), permittivity mapping corresponds to the dense phase of K_{10}-D_{10} condensates showing increasing permittivity with ATP concentration. In (b), the PEG weight fraction is 10 wt%, and the BSA concentration is 0.375 mM. **(c)** Impact of ATP concentration on the permittivity of K_{10}-D_{10}, BSA-PEG (shown in a,b) and glycinin condensates of 10 g/L total protein concentration in 100 mM NaCl (the permittivity values in the absence of ATP are given in Fig. 4).

Figure 5a,c demonstrates that adding just a few mM of ATP progressively increases the permittivity of glycinin and K_{10}-D_{10} condensates by approximately 25 and 15%, respectively. Similar trends are observed in the BSA-PEG system, where the permittivity of the dilute phase increases by 60% upon adding 6.25 mM of ATP, compared to an 8% increase for the dense phase. These results highlight the sensitivity of this method: despite only mild changes in the properties of the dense phase, the reliable detection of permittivity shifts in both phases enables the identification of changes in the mixture’s position on its phase diagram.

Overall, these findings underscore the sensitivity of the proposed method in detecting fine variations in the degree of phase separation and hydration within multi-phase systems, providing a precise and quantitative approach for mapping sample permittivity.

DISCUSSION

The permittivity of biomolecular condensates has recently gained attention as a key parameter for understanding how physiological function of condensates emerges from fundamental biophysics principles [2, 7, 11]. Notably, differences in permittivity between immiscible phases of water-soluble biopolymers was shown to govern their interfacial surface tension [2, 11, 21], ensuring the stability of core-shell layered architectures of nuclear organelles – an essential feature for their biological function [2]. Fundamentally, this interdependence between permittivity mismatch and surface tension arises from the existence of a water activity gradient that separates phases of different permittivity [42, 53, 54]. This gradient imposes an entropic penalty on interfacial water molecules, limiting their conformational degrees of freedom when traveling from a high-permittivity to a lower-permittivity region [42, 53, 54]. Consequently, via the release of water molecules no longer hydrating the condensed proteins, LLPS enables cells to regulate their internal permittivity by locally modulating intracellular water activity [7, 55]. Conversely, changes in water activity can trigger LLPS, allowing cells to adapt to extreme conditions by using released water to buffer changes in cytoplasmic conditions [7, 55].

Molecular dynamics simulation [55-59] further support this perspective demonstrating that water activity and permittivity are intrinsically linked, and highly sensitive to temperature changes. This suggests that biomolecular condensation constitutes an entropically driven feedback response, allowing cells to counterbalance osmotic and thermal perturbations through spontaneous modulation of intracellular dielectric permittivity [7, 21, 55, 58].

Our results show that condensate permittivity alone does not distinguish between different types of interactions driving LLPS, i.e. heterotypic versus homotypic interactions (Figs. 3-5). The structural conformation of scaffold biopolymers can be expected to influence water activity thereby indirectly affecting the dielectric properties of the system. However, the protein-to-water ratio within condensates plays a key role in determining their permittivity. We performed Raman spectroscopy measurements (see Fig. S8), which suggest that the differences in permittivity between R_{10}-D_{10} and K_{10}-D_{10} condensates can indeed be attributed to variations in protein-to-water ratio within the condensed phase. Specifically, the relative Raman intensity of the C-H stretching band (2800-3000 cm^{-1}) compared to the water band (3100-3700) indicates that K_{10}-D_{10} condensates contain a higher portion of water relative to peptide than R_{10}-D_{10} condensates (Fig. S8). This finding aligns with the observed ~$20\varepsilon_0$ increase in the permittivity of K_{10}-D_{10} condensates (Fig. 3).

Interestingly, both the permittivity and the Raman signature of biomolecular condensates were shown to be affected by different types of salts according to the Hofmeister series [14, 21]. While a more extensive investigation on the interplay between condensate permittivity and the vibrational properties of its water content is currently in progress, our results emphasize the potential of our approach to elucidate the complex crosstalk between protein-protein interaction, protein hydration and water activity. Considering that ACDAN is widely used as a probe of water dipolar relaxation *in vivo*, the current study also provides a new framework to explore these properties within the intracellular milieu, where macromolecular crowding and solute composition strongly influence molecular diffusion, signaling, and cellular physiology [15, 29-32].

Beyond the immediate applications outlined above, this method could provide valuable insights into the fundamental mechanisms underlying the recently reported capacitive behavior of biomolecular condensates [60, 61] and further elucidate the role of electrostatics and condensate surface charge in modulating their affinity to membranous compartments [15, 45, 46, 62]. In particular, we speculate that the permittivity of biomolecular condensates may be a key factor governing interactions with membrane interfaces, which are characterized by sharp gradients in water activity. Supporting this idea, a comparison of the permittivity values of the PEG-rich and dextran-rich phases in the PEG-dextran ATPS (Fig. 4a,b) with the evolution of the intrinsic contact angle describing membrane wetting by these condensates [43] at similar PEG and dextran weight fractions reveals a linear correlation between the PEG-dextran permittivity contrast and membrane wetting affinity. Furthermore, given that the hydrophobic core of lipid membranes exhibits a low permittivity similar to that of oils, condensates with lower dielectric permittivity may have a greater tendency to interact with and stabilize membrane defects. This could have implications for cellular repair mechanisms, where condensates act as plugs for transient membrane pores [5, 63]. In this context, condensates with reduced permittivity may be better suited to integrate into the membrane environment, facilitating pore sealing and restoring membrane integrity.

In conclusion, this work demonstrates that ACDAN hyperspectral imaging constitutes a broadband, yet highly sensitive tool for mapping local permittivity in heterogeneous systems. Additionally, the method is particularly convenient considering that most modern commercial confocal microscopes are already equipped for hyperspectral imaging [64]. The approach offers insight into the influence of hydrotropic additives on LLPS. We expect that its application to more complex systems will deepen our understanding of other physiologically-relevant phase transitions and processes, including condensate aging and liquid-to-solid transitions associated with neurodegenerative pathologies [65].

METHODS

Materials

6-acetyl-2-dimethylaminonaphthalene (ACDAN) was purchased from Santa Cruz Biotechnology (USA). Polydiallyldimethylammonium chloride (PDDA, 200-350 kDa, 20 wt% solution in water), adenosine triphosphate (ATP) and sodium hydroxide (NaOH) were obtained from Sigma-Aldrich (Missouri, USA). Poly(ethylene glycol) (PEG 8000, Mw 8kg/mol and PEG 400, Mw 4kg/mol) and dextran from Leuconostoc mesenteroides (molecular weight between 400 kDa and 500 kDa) were purchased from Sigma-Aldrich. The oligopeptides, poly-L-lysine hydrochloride (degree of polymerization, n = 10; K_{10}), poly and poly-L-aspartic acid sodium salt (n = 10; D_{10}) were purchased from Alamanda Polymers (AL, USA) and used without further purification (≥95%). BSA (≥98% purity, 66kg/mol), MBP bovine (≥90%), 1,4-Dioxane, Anisol (99%), 1-Hexanol and 1-Butanol (99.9%) were purchased from Sigma-Aldrich. Mineral oil was purchased from Carl Roth GmbH. Ethanol absolute was purchased from VWR chemicals BDH. Phosphate buffered saline (PBS) pH 7.2 was purchased from Thermofisher. Polyvinyl alcohol (PVA, Mw 145000kg/mol) was purchased from Merck (Darmstadt, Germany). All solutions were prepared using ultrapure water from SG water purification system (Ultrapure Integra UV plus, SG Wasseraufbereitung) with a resistivity of 18.2 MΩ cm.

Condensate formation and labelling

Coverslips for confocal microscopy (26 × 56 mm, Waldemar Knittel Glasbearbeitungs GmbH, Germany) were washed with ethanol and water, then passivated with a 10 mg/mL BSA solution and an aliquot of 10µL of condensates suspension was placed on the coverslip before imaging.

PDDA-ATP condensates: Phase separated droplets were formed by gently mixing aliquots of stock solutions of ATP and PDDA (in this order) with ACDAN in pure water to a final volume of 10 µL. The final concentration of each component was as follows: 14.8 mM ATP, 4.9 mM PDDA, 10µM ACDAN.

Glycinin condensates: Freeze-dried glycinin was a gift from Dr. Nannan Chen. The purification is detailed in ref [47]. A 20 mg/mL glycinin solution at pH 7 was freshly prepared in ultrapure water and filtered with 0.45 µm filters to remove any insoluble materials. To form the condensates, the desired volume of the glycinin solution was mixed with the same volume of a NaCl solution of twice the desired final concentration. In this manner, the final protein concentration was 10 mg/mL [47]. The final concentration of ACDAN was 5µM.

K_{10}-D_{10} and R_{10}-D_{10} condensates: Phase separated droplets were formed by gently mixing aliquots of stock solutions of D_{10} and K_{10} or R_{10} (in this order) with ACDAN in pure water to a final volume of 10 µL. The final concentration of each component was as follows: 2.5 mM D_{10}, 2.5 mM K_{10} or R_{10}, 15µM ACDAN.

PEG-BSA condensates: Phase separated droplets were formed by gently mixing aliquots (via pipetting and releasing 3 times the total volume) in a 1:1 ratio of stock solutions of 20% PEG-

8000 in PBS with 30µM ACDAN with BSA dissolved in PBS at half the desired concentration and to a final volume of 10 µL.

PEG-Dextran condensates: A polymer solution in composed of the desired weight fractions of PEG and dextran were prepared and left, when relevant, for 2 days to completely phase separate and equilibrate. ACDAN was then added to each phase to reach a final concentration of 25µM of ACDAN.

MBP condensates: MBP condensates were prepared by following the procedure described in [66]. Briefly, a 5mg/mL solution of MBP dissolved in water was mixed with a 20mM NaOH solution of 10µM ACDAN in a 1:1 ratio.

Confocal microscopy and hyperspectral imaging

Hyperspectral images were acquired using a confocal Leica SP8 FALCON microscope equipped with a 63×, 1.2 NA water immersion objective (Leica, Mannheim, Germany). The microscope was coupled to a pulsed Ti:Sapphire laser MaiTai (SpectraPhysics, USA), with a repetition rate of 80 MHz. A two-photon wavelength of 780 nm was used for ACDAN excitation. Image acquisition was performed with a frame size of 512 × 512 pixels [15, 46] and a pixel size of 72 nm×72 nm using a Hyd SMD detector in standard mode. For hyperspectral imaging, the xyλ configuration of Leica SP8 was used, sequentially measuring in 32 channels with a bandwidth of 9.75 nm in the range from 416 to 728 nm. Some hyperspectral images were realigned using the ImageJ software and all hyperspectral stacks were processed by the SimFCS software developed at the Laboratory of Fluorescence Dynamics (available at https://www.lfd.uci.edu/globals/), and analyzed using Python code based in the PhasorPy library (available at https://www.phasorpy.org/).

Spectrofluorimeter measurements

Bulk fluorescence measurements were made using a FluoroMax4® (HORIBA Scientific) fluorimeter with the FluorEssence (V3.5) software. The excitation wavelength was set to 360nm with an excitation slit width of 5nm and a detection slit width of 2nm. Data acquisition was performed at 25°C using a 1nm detection wavelength increment over a (375-700) nm spectral window for mineral oil samples and over a (400-700) nm spectral window for the remaining samples. Quartz chambers (Hellma® Analytics) were used to perform all measurements, chamber volumes of 50µL were used for measuring the emission of ACDAN in water-dioxane mixtures, ethanol 100% and butanol 100%, 200µL for measuring the emission of ACDAN in PEG400-water mixtures and 2.8mL for measuring the emission of ACDAN in anisol-hexanol mixtures and mineral oil. The measurement of each condition consisted in three independent trials which were then averaged and the error was computed by performing an error propagation analysis accounting for the slit parameters and the standard deviations associated with each trial triplet. The ACDAN concentration was 1µM for all measurements.

Raman measurements

Raman spectra were acquired with a Raman confocal microscope Alpha300 R (WITec GmbH, Germany) with Zeiss EC Epiplan 50×, 0.75NA objective, at an excitation wavelength of 532 nm and 50 mW laser power. Spectra were acquired in the range 400–4100 cm^{-1}, each acquisition consisted of an average of seven successive acquisitions performed over a 10s integration timespan. The Raman band of the silicon wafer was used to calibrate the spectrometer. Data were analyzed with the Project FIVE v.5.2 data evaluation software from WITec, and the background was interpolated and subtracted using the OriginPro2023 software via the built-in baseline subtraction procedure.

Gaussian fit analysis

The Gaussian fit analysis of ACDAN hyperspectral imaging data consists in approximating the wavelength-intensity profile of ACDAN emission by a skewed Gaussian function of the form:

$$I(\lambda) = I_0\, \Psi\left(\frac{\lambda-\mu}{\sigma}\right)\, \Phi\left(\gamma\left(\frac{\lambda-\mu}{\sigma}\right)\right), \tag{M1}$$

$$\Psi(x) = \frac{1}{\sqrt{2\pi}} \exp\left(-\frac{x^2}{2}\right), \tag{M2}$$

$$\Phi(x) = \frac{1}{2}\left(1 + \operatorname{erf}\left(\frac{x}{\sqrt{2}}\right)\right), \tag{M3}$$

where Ψ, Φ, erf, λ, μ, σ, I_0 and γ respectively represent the normal distribution function, the cumulative distribution function, the error function, the wavelength, the mean wavelength, the mean deviation, the intensity scaling factor and the skewness factor. Data interpolation was performed based on computer programing script written in Python and based on the scipy library. The λ_{max} was then evaluated based on the position of the maximum of the fitted ACDAN emission curve and used as an input in the $\lambda - \varepsilon$ calibration curves presented in Figs. 1B and 2B in the main text.

Spectral phasor analysis

The spectral phasor analysis of ACDAN hyperspectral imaging data consists in calculating the real and imaginary components of the Fourier transform, respectively referred to as G and S, and using them as Cartesian coordinates on a 2D spectral phasor map. (G, S) are defined by the following expressions:

$$G = \frac{\int_{\lambda_0}^{\lambda_f} I(\lambda)\cos\big(\omega n(\lambda-\lambda_0)\big)\mathrm{d}\lambda}{\int_{\lambda_0}^{\lambda_f} I(\lambda)\mathrm{d}\lambda}, \tag{M4}$$

$$S = \frac{\int_{\lambda_0}^{\lambda_f} I(\lambda)\sin\big(\omega n(\lambda-\lambda_0)\big)\mathrm{d}\lambda}{\int_{\lambda_0}^{\lambda_f} I(\lambda)\mathrm{d}\lambda}, \tag{M5}$$

where $I(\lambda)$ for a particular pixel represents the intensity as a function of wavelength, measured in the interval $(\lambda_0; \lambda_f)$. This range depends on instrumental constraints and the type of detector used for the analysis, in our case 416–728 nm. Note that changing the detection range will necessarily results in a change of the relative positions of different points on the phasor plot; therefore, the detection range must be conserved across all experiments in order to be able to compare measurements. The parameter n is the harmonic, i.e. the number of cycles of the trigonometric function that are fit in the wavelength range by means of the angular frequency ω:

$$\omega = \frac{2\pi}{(\lambda-\lambda_0)} \tag{M6}$$

When imaging with a microscope, we acquire a discrete number of spectral steps corresponding to the number of detection windows that cover the spectral range. For computational purposes, the spectral phasor transform is expressed as a discretized approximation of the continuous transform as:

$$G = \frac{\sum_c^{N_c} I(c)\cos(2\pi c/N_c)}{\sum_c^{N_c} I(c)}, \tag{M7}$$

$$S = \frac{\sum_c^{N_c} I(c)\sin(2\pi c/N_c)}{\sum_c^{N_c} I(c)}, \tag{M8}$$

where $I(c)$ is the pixel intensity at channel and c is the total number of channels. Conveniently, even if the total number of spectral acquisition channels is small (in our case 32), the coordinates S and G can be considered quasi-continuous, since the photon counts in each pixel and channel are high enough (~102) to allow a wide range of possible values of the coordinates S and G.

The spectral phasor approach obeys the rules of vector algebra, known as the linear combination of phasors. This property implies that a combination of two independent fluorescent species will appear on the phasor plot at a position that is a linear combination of the phasor positions of the two independent spectral species. The fraction of each component can be determined from the coefficients of the linear combination.

Note that the phase angle ϕ, and the modulation, M can be obtained through:

$$\phi = \arctan\left(\frac{S}{G}\right) \tag{M9}$$

$$M = \sqrt{S^2 + G^2} \tag{M10}$$

Data processing and spectral phasor analysis were performed by first converting the Image stacks into .r64 files using the SimFCS software developed at the Laboratory of Fluorescence Dynamics, available on the webpage (https://www.lfd.uci.edu/globals/), and further processed using Python programming code based on the PhasorPy library (https://www.phasorpy.org/).

DATA AVAILABILITY STATEMENT

The source data underlying Figs. 1B-C, 2B-C, 3A-D, 4B, 4D-G, 5A-E as well as Supplementary Figs. 1B-C, 2A-D, 3A-D, 4A–C, 5, 6A-B, 7 and 8 are provided in a separate Excel file labelled 'Source Data' with this paper.

ACKNOWLEDGEMENTS

A.M. acknowledges support from Alexander von Humboldt Foundation. We acknowledge Nannan Chen for providing glycinin, and Clemens Schmitt for the assistance with Raman experiments. We also acknowledge support from the German Academic Exchange Service (Deutscher Akademischer Austauschdienst, DAAD) in the framework of project 57654674.

REFERENCES

1. Decker, C.J. & Parker, R. P-bodies and stress granules: possible roles in the control of translation and mRNA degradation. *Cold Spring Harbor perspectives in biology* **4**, a012286 (2012).
2. Feric, M. et al. Coexisting Liquid Phases Underlie Nucleolar Subcompartments. *Cell* **165**, 1686-1697 (2016).
3. Feric, M. et al. Mesoscale structure–function relationships in mitochondrial transcriptional condensates. *Proceedings of the National Academy of Sciences* **119**, e2207303119 (2022).
4. Fei, J. et al. Quantitative analysis of multilayer organization of proteins and RNA in nuclear speckles at super resolution. *Journal of cell science* **130**, 4180-4192 (2017).
5. Bussi, C. et al. Stress granules plug and stabilize damaged endolysosomal membranes. *Nature* **623**, 1062-1069 (2023).
6. Alberti, S. & Hyman, A.A. Biomolecular condensates at the nexus of cellular stress, protein aggregation disease and ageing. *Nature Reviews Molecular Cell Biology* **22**, 196-213 (2021).
7. Watson, J.L. et al. Macromolecular condensation buffers intracellular water potential. *Nature* **623**, 842-852 (2023).
8. Lyon, A.S., Peeples, W.B. & Rosen, M.K. A framework for understanding the functions of biomolecular condensates across scales. *Nat Rev Mol Cell Biol* **22**, 215-235 (2021).
9. Smokers, I.B., Visser, B.S., Slootbeek, A.D., Huck, W.T. & Spruijt, E. How Droplets Can Accelerate Reactions– Coacervate Protocells as Catalytic Microcompartments. *Accounts of Chemical Research* **57**, 1885-1895 (2024).
10. Jawerth, L. et al. Protein condensates as aging Maxwell fluids. *Science* **370**, 1317-1323 (2020).
11. Ye, S. et al. Micropolarity governs the structural organization of biomolecular condensates. *Nature Chemical Biology* **20**, 443-451 (2024).
12. Abyzov, A., Blackledge, M. & Zweckstetter, M. Conformational dynamics of intrinsically disordered proteins regulate biomolecular condensate chemistry. *Chemical Reviews* **122**, 6719-6748 (2022).

13. Boeynaems, S. et al. Spontaneous driving forces give rise to protein− RNA condensates with coexisting phases and complex material properties. *Proceedings of the National Academy of Sciences* **116**, 7889-7898 (2019).
14. Joshi, A. et al. Hydrogen-Bonded Network of Water in Phase-Separated Biomolecular Condensates. *The Journal of Physical Chemistry Letters* **15**, 7724-7734 (2024).
15. Mangiarotti, A. et al. Biomolecular condensates modulate membrane lipid packing and hydration. *Nature Communications* **14**, 6081 (2023).
16. Dogra, P., Joshi, A., Majumdar, A. & Mukhopadhyay, S. Intermolecular charge-transfer modulates liquid–liquid phase separation and liquid-to-solid maturation of an intrinsically disordered pH-responsive domain. *Journal of the American Chemical Society* **141**, 20380-20389 (2019).
17. Dai, Y. et al. Interface of biomolecular condensates modulates redox reactions. *Chem* **9**, 1594-1609 (2023).
18. Schlüßler, R. et al. Correlative all-optical quantification of mass density and mechanics of subcellular compartments with fluorescence specificity. *Elife* **11**, e68490 (2022).
19. Hong, Y. et al. Label-free quantitative analysis of Coacervates via 3D phase imaging. *Advanced Optical Materials* **9**, 2100697 (2021).
20. Linsenmeier, M. et al. Dynamic arrest and aging of biomolecular condensates are modulated by low-complexity domains, RNA and biochemical activity. *Nature Communications* **13**, 3030 (2022).
21. Zhu, L., Pan, Y., Hua, Z., Liu, Y. & Zhang, X. Ionic Effect on the Microenvironment of Biomolecular Condensates. *Journal of the American Chemical Society* (2024).
22. Wang, L. et al. Xanthone-based solvatochromic fluorophores for quantifying micropolarity of protein aggregates. *Chemical Science* **13**, 12540-12549 (2022).
23. Xiao, H., Li, P. & Tang, B. Recent progresses in fluorescent probes for detection of polarity. *Coordination Chemistry Reviews* **427**, 213582 (2021).
24. Levitt, J.A., Chung, P.-H. & Suhling, K. Spectrally resolved fluorescence lifetime imaging of Nile red for measurements of intracellular polarity. *Journal of biomedical optics* **20**, 096002-096002 (2015).
25. Yang, Z. et al. A Nile Red/BODIPY-based bimodal probe sensitive to changes in the micropolarity and microviscosity of the endoplasmic reticulum. *Chemical Communications* **50**, 11672-11675 (2014).
26. Cui, J. et al. Mitochondria-targeted ratiometric fluorescent probes for micropolarity and microviscosity and their applications. *Chinese Chemical Letters* **30**, 1071-1074 (2019).
27. Weber, G. & Farris, F.J. Synthesis and spectral properties of a hydrophobic fluorescent probe: 6-propionyl-2-(dimethylamino) naphthalene. *Biochemistry* **18**, 3075-3078 (1979).
28. Gunther, G., Malacrida, L., Jameson, D.M., Gratton, E. & Sánchez, S.A. LAURDAN since Weber: the quest for visualizing membrane heterogeneity. *Accounts of chemical research* **54**, 976-987 (2021).
29. Thoke, H.S. et al. Tight coupling of metabolic oscillations and intracellular water dynamics in Saccharomyces cerevisiae. *PLoS One* **10**, e0117308 (2015).
30. Thoke, H.S., Thorsteinsson, S., Stock, R.P., Bagatolli, L.A. & Olsen, L.F. The dynamics of intracellular water constrains glycolytic oscillations in Saccharomyces cerevisiae. *Scientific Reports* **7**, 16250 (2017).
31. Begarani, F. et al. Capturing metabolism-dependent solvent dynamics in the lumen of a trafficking lysosome. *ACS nano* **13**, 1670-1682 (2019).
32. Vorontsova, I. et al. In vivo macromolecular crowding is differentially modulated by aquaporin 0 in zebrafish lens: Insights from a nanoenvironment sensor and spectral imaging. *Science Advances* **8**, eabj4833 (2022).
33. Bagatolli, L.A. To see or not to see: Lateral organization of biological membranes and fluorescence microscopy. *Biochim. Biophys. Acta-Biomembr.* **1758**, 1541-1556 (2006).
34. Patel, A. et al. ATP as a biological hydrotrope. *Science* **356**, 753-756 (2017).

35. Sato, T., Niwa, H., Chiba, A. & Nozaki, R. Dynamical structure of oligo (ethylene glycol) s-water solutions studied by time domain reflectometry. *The Journal of chemical physics* **108**, 4138-4147 (1998).
36. Chaube, H., Rana, V. & Gadani, D. Dielectric absorption in mixtures of anisole with some primary alcohols at microwave frequency. *Philosophical Magazine* **91**, 4465-4473 (2011).
37. Badicu, L., Notingher, P., Dumitran, L., Tanasescu, G. & Popa, D. in Proceedings of the 5th International Conference Metrology & Measurement Systems 284-289 (2009).
38. Critchfield, F.E., Gibson Jr, J.A. & Hall, J.L. Dielectric constant for the dioxane—water system from 20 to 35°. *Journal of the American Chemical Society* **75**, 1991-1992 (1953).
39. Lakowicz, J. Principles of fluorescence spectroscopy. *University of Maryland School of Medicine Baltimore* **132** (2006).
40. Scholte, T.G. A contribution to the theory of the dielectric constant of polar liquids. *Physica* **15**, 437-449 (1949).
41. Gebhart, S.C., Majumder, S.K. & Mahadevan-Jansen, A. Comparison of spectral variation from spectroscopy to spectral imaging. *Applied optics* **46**, 1343-1360 (2007).
42. Socas, L.B.P. & Ambroggio, E.E. Linking surface tension to water polarization with a new hypothesis: The Ling-Damodaran Isotherm. *Colloids and Surfaces B: Biointerfaces* **230**, 113515 (2023).
43. Liu, Y., Agudo-Canalejo, J., Grafmüller, A., Dimova, R. & Lipowsky, R. Patterns of Flexible Nanotubes Formed by Liquid-Ordered and Liquid-Disordered Membranes. *ACS Nano* **10**, 463-474 (2016).
44. Liu, Y., Lipowsky, R. & Dimova, R. Concentration Dependence of the Interfacial Tension for Aqueous Two-Phase Polymer Solutions of Dextran and Polyethylene Glycol. *Langmuir* **28**, 3831-3839 (2012).
45. Lu, T., Hu, X., van Haren, M.H., Spruijt, E. & Huck, W.T. Structure-Property Relationships Governing Membrane-Penetrating Behaviour of Complex Coacervates. *Small* **19**, 2303138 (2023).
46. Mangiarotti, A., Chen, N., Zhao, Z., Lipowsky, R. & Dimova, R. Wetting and complex remodeling of membranes by biomolecular condensates. *Nature Commun.* **14**, 2809 (2023).
47. Chen, N., Zhao, Z., Wang, Y. & Dimova, R. Resolving the Mechanisms of Soy Glycinin Self-Coacervation and Hollow-Condensate Formation. *ACS Macro Letters* **9**, 1844-1852 (2020).
48. Smolin, N., Oleinikova, A., Brovchenko, I., Geiger, A. & Winter, R. Properties of spanning water networks at protein surfaces. *The Journal of Physical Chemistry B* **109**, 10995-11005 (2005).
49. Nakasako, M. Water–protein interactions from high–resolution protein crystallography. *Philosophical Transactions of the Royal Society of London. Series B: Biological Sciences* **359**, 1191-1206 (2004).
50. Lamy, H. et al. Kinetic Study of the Esterase-like Activity of Albumin following Condensation by Macromolecular Crowding. *Biomacromolecules* **25**, 2803-2813 (2024).
51. Kunz, W., Holmberg, K. & Zemb, T. Hydrotropes. *Current Opinion in Colloid & Interface Science* **22**, 99-107 (2016).
52. Saurabh, S. et al. ATP-responsive biomolecular condensates tune bacterial kinase signaling. *Sci Adv* **8**, eabm6570 (2022).
53. Kumar, R., Sumpter, B.G. & Muthukumar, M. Enhanced Phase Segregation Induced by Dipolar Interactions in Polymer Blends. *Macromolecules* **47**, 6491-6502 (2014).
54. Ling, G.N. Life at the cell and below-cell level: The hidden history of a fundamental revolution in biology. (Pacific Press New York, 2001).
55. Mukherjee, S. & Schäfer, L. (2023).
56. Chen, S. & Wang, Z.-G. Driving force and pathway in polyelectrolyte complex coacervation. *Proceedings of the National Academy of Sciences* **119**, e2209975119 (2022).
57. Ylitalo, A.S., Balzer, C., Zhang, P. & Wang, Z.-G. Electrostatic correlations and temperature-dependent dielectric constant can model LCST in polyelectrolyte complex coacervation. *Macromolecules* **54**, 11326-11337 (2021).

58. Wessén, J., Pal, T., Das, S., Lin, Y.-H. & Chan, H.S. A Simple Explicit-Solvent Model of Polyampholyte Phase Behaviors and Its Ramifications for Dielectric Effects in Biomolecular Condensates. *The Journal of Physical Chemistry B* **125**, 4337-4358 (2021).
59. Workman, R.J. & Pettitt, B.M. Thermodynamic Compensation in Peptides Following Liquid–Liquid Phase Separation. *The Journal of Physical Chemistry B* **125**, 6431-6439 (2021).
60. Posey, A.E. et al. Biomolecular condensates are characterized by interphase electric potentials. *Journal of the American Chemical Society* **146**, 28268-28281 (2024).
61. Dai, Y., Wang, Z.-G. & Zare, R.N. Unlocking the electrochemical functions of biomolecular condensates. *Nature Chemical Biology*, 1-14 (2024).
62. Mangiarotti, A., Schmidt, K.V., Lipowsky, R. & Dimova, R. Lipid packing and cholesterol content regulate membrane wetting by biomolecular condensates. *bioRxiv*, 2024.2007. 2015.603610 (2024).
63. Janssen, A.F.J. et al. Patching up the nucleus: a novel role for PMLII in nuclear envelope rupture repair. *bioRxiv*, 2025.2001.2024.634656 (2025).
64. Zimmermann, T., Rietdorf, J. & Pepperkok, R. Spectral imaging and its applications in live cell microscopy. *FEBS Lett* **546**, 87-92 (2003).
65. Patel, A. et al. A liquid-to-solid phase transition of the ALS protein FUS accelerated by disease mutation. *Cell* **162**, 1066-1077 (2015).
66. Aggarwal, S. et al. Myelin membrane assembly is driven by a phase transition of myelin basic proteins into a cohesive protein meshwork. *PLoS biology* **11**, e1001577 (2013).